Biomechanics and Modeling in Mechanobiology (2026) 25:39
https://doi.org/10.1007/s10237-026-02062-w

ORIGINAL PAPER

In silico analysis of the invasion mechanics and invasiveness of the Plasmodium falciparum merozoite

Chimwemwe Msosa[1,2] · **Tamer Abdalrahman**[1,3] · **Thomas Franz**[1,4]

Received: 23 June 2025 / Accepted: 6 March 2026 / Published online: 17 April 2026

Abstract

Although there has been considerable progress in understanding the factors that determine the invasiveness of Plasmodium falciparum merozoites, the collective role of the biophysical characteristics of erythrocyte deformability in the invasion process is poorly understood. Cell shape, cytoplasmic viscosity, and membrane stability are the main determinants of erythrocyte deformability, but it remains unknown how these properties affect the merozoite invasiveness. This study aimed to investigate computationally (i) the role of erythrocyte morphology and merozoite-induced erythrocyte membrane damage in merozoite invasion and (ii) the suitability of mechanical markers of merozoite-induced erythrocyte membrane damage for screening of invasion-blocking antimalarial drugs. Finite element models were developed to represent a human erythrocyte and a spherocyte, their invasion by a malaria merozoite, and erythrocyte compression and nanoindentation as mechanical assays for membrane damage. Smoothed particle hydrodynamics represented the erythrocyte cytoplasm, and merozoite-induced erythrocyte membrane damage was implemented with a constitutive model. The invasiveness of the merozoite decreases with increased erythrocyte sphericity associated with genetic disorders such as hereditary spherocytosis. The invasiveness is larger when membrane damage is induced in the erythrocyte at an early invasion stage than throughout the invasion process. The minimum force required for a malaria merozoite to invade a human erythrocyte was predicted to be 11 pN. The findings on the invasion mechanics can guide future studies into the invasiveness of the merozoite. The nanoindentation simulations point to the potential of nanoindentation to determine erythrocyte membrane damage for screening novel invasion-blocking antimalarial drugs.

Keywords Erythrocyte · Hereditary spherocytosis · Malaria · Finite element method · Smoothed particle hydrodynamics · Drug screening

1 Introduction

The invasion of malaria merozoites into human erythrocytes has been extensively studied as a potential target for antimalarial drugs (Flannery et al. 2013). During the invasion of erythrocytes, the merozoite is highly exposed to the host immune system and is highly vulnerable to therapeutic interventions; hence, it is an essential target for antimalarial drugs. Despite the considerable interest in studying the invasion process, fundamental gaps remain in our understanding of the invasion process. Despite decades of research, an incomplete understanding of the disease's physiopathology continues to hinder eradication efforts. Beyond oxidative stress-mediated damage (Percário et al. 2012), erythrocyte invasion by the Plasmodium falciparum merozoite involves highly coordinated ligand–receptor interactions that induce erythrocyte membrane remodelling. The binding of parasite

✉ Thomas Franz
thomas.franz@uct.ac.za

Chimwemwe Msosa
cmsosa@mubas.ac.mw

1 Biomedical Engineering Research Centre, Division of Biomedical Engineering, Department of Human Biology, University of Cape Town, Observatory 7925, South Africa

2 Department of Electrical Engineering, Faculty of Engineering, Malawi University of Business and Applied Sciences, Blantyre, Malawi

3 Architecture, Construction and Engineering, International University of Applied Sciences, 10247 Berlin, Germany

4 Bioengineering Science Research Group, Engineering Sciences, Faculty of Engineering and Physical Sciences, University of Southampton, Southampton SO171BJ, UK

ligands such as EBA-175 to glycophorin A activates intracellular phosphorylation cascades involving cytoskeletal proteins, leading to altered mechanical properties of the erythrocyte membrane (Sisquella et al. 2017). Pharmacological inhibition of this remodelling pathway has been shown to suppress phosphorylation cascades, limit changes in membrane deformability, and block merozoite invasion, emphasising the importance of host membrane mechanics in conditioning erythrocytes for successful parasite entry (Sisquella et al. 2017). To date, the impact of erythrocyte morphology and local erythrocyte membrane damage on the invasiveness of merozoites has not been comprehensively explored due to the lack of appropriate and detailed invasion mechanics models. As such, in silico invasion mechanics models offer an alternative approach for investigating the invasiveness of the merozoite, complementing in vitro and in vivo studies.

Various in silico models have been developed to describe erythrocyte mechanics. These include cortical shell Newtonian liquid drop models applied to biological cells such as erythrocytes (Lim et al. 2006), finite element models of erythrocyte deformation under shear stress (Ahmad & Ahmad 2015), and microstructural representations of the erythrocyte spectrin network (Fai et al. 2017). Multiscale approaches based on dissipative particle dynamics have further enabled simulation of infected erythrocyte deformation across intra-erythrocytic developmental stages by coupling subcellular and vascular-scale mechanics. More recently, atomistically enriched constitutive models combined with mesh-free numerical methods have demonstrated improved predictive accuracy of erythrocyte deformability (Ademiloye et al. 2018). However, despite these advances, none of these models have been applied to investigate the invasion mechanics of malaria parasites partly due to limited validation data for mechanical and other multiscale models.

The merozoite entry into an erythrocyte is an active process that involves the application of actomyosin-based forces on the erythrocyte membrane. The forces are transmitted to the erythrocyte membrane through contact with the merozoite surface (Dasgupta et al. 2014). To date, a detailed analysis of the mechanistic role of the erythrocyte membrane and associated structure, i.e. the spectrin network involved in the invasion process, is limited to 2D analytical models (Abdalrahman & Franz 2017). Additionally, current analytical models do not incorporate large deformations and remodelling of the erythrocyte membrane, which limits their application to early-stage invasion with a maximum invagination depth of 10% of the merozoite length. Thus, there is a need to develop realistic 3D invasion models that account for all factors that determine the merozoite invasiveness, i.e. merozoite-induced membrane damage.

Hereditary spherocytosis is caused by genetic alteration of erythrocyte membrane proteins, leading to the formation of spherocytes. Previously, it has been documented that cells with hereditary spherocytosis have abnormal protein structure and thus have a low susceptibility to infection by the merozoite (Eber & Lux 2004). Despite this finding, little is known about the higher invasion resistance of these cells.

The current study aimed to computationally investigate the erythrocyte mechanics during malaria parasite invasion with an emphasis on (i) the factors contributing to the merozoite invasiveness and (ii) the impact of local disruption of the spectrin network on the global mechanical properties of the erythrocyte for assessing the feasibility of mechanical markers for testing the efficacy of invasion-blocking antimalarial drugs.

2 Materials and methods

2.1 Geometric modelling

2.1.1 Healthy erythrocyte

The initial biconcave geometry of the erythrocyte is defined by the following equation (Evans & Fung 1972):

$$z = \pm D_0 \left(1 - \frac{4\left(x^2 + y^2\right)}{D_0^2}\right)^{1/2} \left(a_0 + a_1 \frac{x^2 + y^2}{D_0^2} + a_2 \frac{\left(x^2 + y^2\right)^2}{D_0^4}\right) \tag{1}$$

with principal coordinate directions x, y, z, the diameter of the undeformed erythrocyte $D_0 = 7.82$ µm, and shape parameters $a_0 = 0.0518$, $a_1 = 2.026$ and $a_2 = -4.491$ (Fig. 1a). The generated erythrocyte model has a volume of 94.47 µm^3 and a surface area of 135 µm^2 consistent with the literature (Li et al. 2014).

2.1.2 Spherocyte

In individuals with spherocytosis, erythrocytes take a spherical form due to alterations of erythrocyte membrane proteins. The geometry was described with

$$r^2 = \left(x - k_c\right)^2 + \left(y - l_c\right)^2 + \left(z - n_c\right)^2 \tag{2}$$

where $r = 2.66$ µm is the radius of the spherocyte (Li et al. 2016) and k_c, l_c, n_c are centre coordinates of the spherocyte, where $k_c = l_c = n_c = 0$. x, y, and z denote the coordinate points on the surface of the spherocyte (Fig. 1b). The surface area-to-volume ratio is 14% smaller for the spherical shape than the discoid geometry.

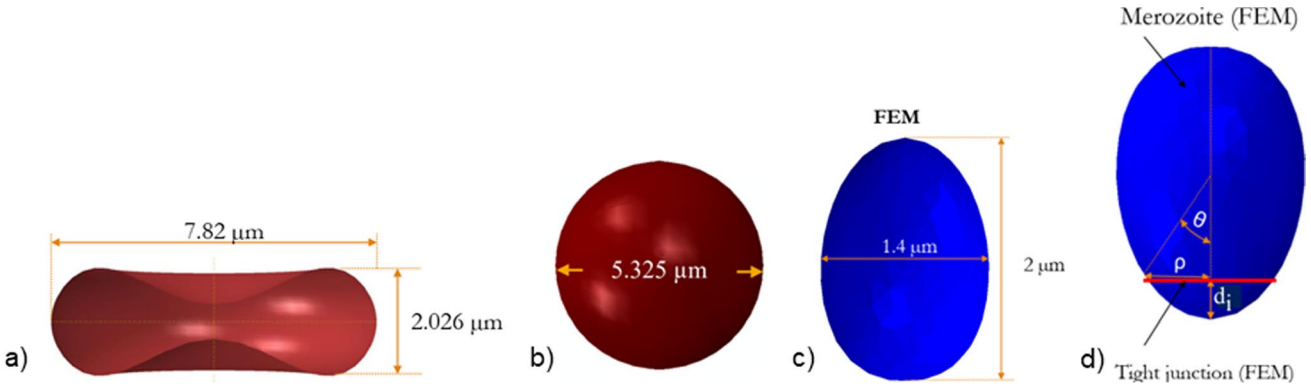

Fig. 1 **a** Erythrocyte geometry, **b** spherocyte geometry, **c** dimension of Plasmodium falciparum merozoite based on cryo-EM data from Dasgupta et al. (2014, Fig. 2), **d** Geometry of rigid egg-shaped merozoite used in the current study

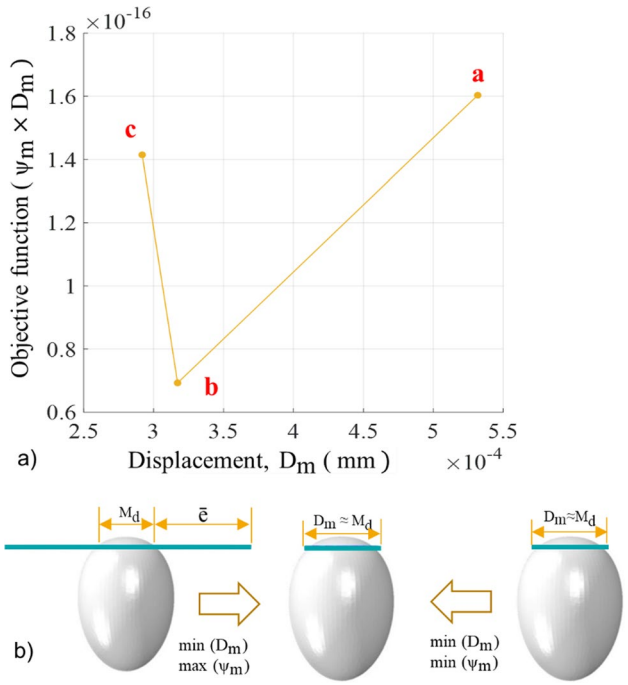

Fig. 2 Illustration of **a** the minimisation process of the objective function and **b** the determination of the Mooney–Rivlin parameters

2.1.3 Plasmodium falciparum merozoite

The merozoite shape has been previously described based on cryo-X-ray images of free merozoites (Dasgupta et al. 2014, Fig. 2). From these data, the mean physical dimensions of the merozoite were determined as follows: length $L_m = 1.98 \pm 0.08$ µm, width $W = 1.40 \pm 0.06$ µm, volume $V_{actual} = 1.71 \pm 0.15$ µm^3, and surface area $A_{actual} = 8.06 \pm 0.72$ µm^2 (Fig. 1c). The 3D merozoite geometry (Fig. 1d) was generated with

$$z(\theta) = [2R_a - R_b(1 - \cos\theta)](1 + \cos\theta)/4 \quad (3)$$

$$\rho(\theta) = \sin\theta[2R_a - R_b(1 - \cos\theta)]/4 \quad (4)$$

where ρ and z are Cartesian coordinates, $R_a = 1$ µm, $R_b = 0.7$ µm are parameters that determine the egg shape profile of the merozoite, and θ is a polar angle with $0° \leq \theta \leq 180°$.

Images from electron microscopy, cryo-electron tomography, cryo-X-ray tomography and widefield deconvolution fluorescence imaging of a merozoite during invasion show negligible changes in merozoite shape throughout the invasion process (Zuccala et al. 2016). Hence, this study treated the merozoite geometry as a rigid body.

2.1.4 Tight junction between the merozoite and erythrocyte membrane

The merozoite pulls itself into the erythrocyte through the tight junction complexes, which it establishes after forming the invasion pit (Pinder et al. 2000; Preiser et al. 2000; Riglar et al. 2011). The tight junction was modelled as a deforming mechanical link between the merozoite surface and the erythrocyte membrane, forming an annulus-like structure to facilitate erythrocyte membrane wrapping. The annulus is defined as a circular ring with an internal diameter of 0.76 µm and a cross-sectional radius of 0.04 µm (Fig. 1d).

2.2 Constitutive modelling

2.2.1 Erythrocyte membrane with merozoite-induced damage

During merozoite invasion, the erythrocyte membrane deformation was considered as mainly due to the mechanical

loads exerted by the merozoite's actomyosin machinery and other external sources, such as blood pressure, whereas the entropic deformation was considered negligible. Hence, the Helmholtz free energy function for the erythrocyte membrane deformation was only represented as internal strain energy.

The damage induced by the merozoite was modelled by modifying the strain energy density function of the erythrocyte membrane. Since the erythrocyte membrane comprises primarily an elastic spectrin network and can be considered an elastic, isotropic, and nearly incompressible continuum, the strain energy density function is usually presented in a decoupled form comprising deviatoric and isochoric terms (Li 2016).

The combination of incompressibility and large deformation of a nearly incompressible hyperelastic material presents difficulties for a displacement-based finite element method as the constraint $J = \det \mathbf{F} = 1$ on the deformation field is highly nonlinear (Weiss 1994). To overcome this challenge, a displacement-based finite element scheme must invoke a small change measure of volumetric deformation. Consequently, the deformation gradient was decomposed into the dilatational and deviatoric parts to apply separate numerical treatments to each part (Weiss 1994).

Therefore, the deformation gradient $\mathbf{F}$ (Gilson & Crabb 2009) and the left Cauchy–Green strain tensor $\mathbf{B}$ were divided into the volume-changing (dilatational) and the volume-preserving (distortional) parts, an approach often used in elasto-plasticity (Ogden 1978). The strain energy density function of the isotropic erythrocyte membrane was expressed in terms of the left Cauchy deformation tensor as

$$\mathbf{B} = \mathbf{F} \cdot \mathbf{F}^{\mathbf{T}} \tag{5}$$

With $\mathbf{F} = \mathbf{R}\ \mathbf{U}$ and $\mathbf{F}^{\mathrm{T}} = \mathbf{R}^{\mathrm{T}}\ \mathbf{U}^{\mathrm{T}}$, where $\mathbf{R}$ is a rotation matrix, and $\mathbf{U}$ is a stretch tensor, Eq. (5) becomes

$$\mathbf{B} = \mathbf{R}\mathbf{U} \cdot \mathbf{U}^{\mathbf{T}}\mathbf{R}^{\mathbf{T}} = \mathbf{U} \cdot \mathbf{U}^{\mathbf{T}}, \tag{6}$$

showing that the left Cauchy deformation tensor $\mathbf{B}$ is a stretch tensor and isotropic.

Hence, the strain energy density function ψ of a damaged erythrocyte membrane can be written in terms of invariants of the left Cauchy–Green deformation tensor:

$$\psi\left(I_1, I_2, J, \tau\right) = R_d\left[\psi_0\left(I_1, I_2\right) + \psi_0(J)\right] \tag{7}$$

with

$I_1 = \mathrm{tr}(\mathbf{B})$,

$I_2 = \frac{1}{2}\left(I_1^2 - \mathrm{tr}\left(\mathbf{B}^2\right)\right)$, and

$J = \sqrt{\det(\mathbf{B})}$,

where $\mathbf{B}$ is the left Cauchy–Green tensor, R_{d} is the damage parameter, ψ_0 is the strain energy density of an intact erythrocyte membrane, I_1 and I_2 are the first and second deviatoric strain invariants, respectively, while J represents the determinant of the deformation gradient and quantifies the local volumetric change, and τ is the indentation time in seconds.

A continuum damage mechanics framework for material stiffness deterioration suitable for implementation in Abaqus Explicit was used to simulate chemical damage induced by a merozoite during the entry process. The model draws on concepts from various strain-based damage models for soft biological materials and biodegradable polymers, which describe constitutive hydrolytic degradation and time-dependent behaviour (Vieira et al. 2011).

R_{d} is a function of chemical and mechanical damage parameters defined as:

$$R_d(\mathbf{B}, J, \tau) = \left[1 - \beta_2\right] e^{-\left(\beta_1 \tau + \beta_2 \psi_0\right)} \tag{8}$$

where $\mathbf{B}$ and J denote the left Cauchy–Green tensor and the volumetric strain of the intact erythrocyte membrane, respectively, τ is the indentation time, and ψ_0 is the strain energy density per reference volume of the intact erythrocyte membrane, β_1 is the chemical damage parameter, and β_2 is the mechanical damage parameter.

For $\beta_2 = 0$, the damage mode is purely chemical, i.e. damage to the erythrocyte membrane is not due to deformation. Thus, β_1 represents chemical damage due to various amounts of phosphorylation, and β_2 represents mechanical damage associated with the tearing or rupturing of the protein chains in the erythrocyte membrane skeleton. The erythrocyte's membrane near incompressibility was defined with a Poisson's ratio $\nu = 0.499$. For incompressible materials, the contribution of the volumetric strain energy density function is neglected since $J = 1$. Since the erythrocyte membrane is nearly incompressible, the deviatoric strain invariants are:

$$\bar{I}_1 = J^{-2/3} I_1 \tag{9}$$

$$\bar{I}_2 = J^{-4/3} I_2. \tag{10}$$

The variation of the strain energy potential δW_i is, by definition, equal to the internal virtual work per reference volume V_0 and can be written as (Dassault Systèmes Simulia Corp 2015):

$$\delta W_i = \int J\left(\mathbf{S} : \delta\mathbf{e} - p\delta\boldsymbol{\epsilon}^{\mathbf{vol}}\right)\mathrm{d}V^0 = \int \delta\psi \mathrm{d}V^0 \tag{11}$$

where

$$\delta\psi = 2\left[\left(\frac{\partial\psi}{\partial\bar{I}_1} + \bar{I}_1\frac{\partial\psi}{\partial\bar{I}_2}\right)\mathbf{B}^* - \frac{\partial\psi}{\partial\bar{I}_2}\mathbf{B}^*\cdot\mathbf{B}^*\right] : \delta\mathbf{e} + J\frac{\partial\psi}{\partial J}\delta\boldsymbol{\epsilon}^{\mathbf{vol}} \tag{12}$$

$$\delta\mathbf{e} = \delta\mathbf{D} - \frac{1}{3}\delta\boldsymbol{\epsilon}^{\mathbf{vol}}I \tag{13}$$

$$\delta\mathbf{D} = \mathrm{sym}(\delta\mathbf{L}) = \frac{1}{2}\left(\delta\mathbf{L} + \delta\mathbf{L}^{\mathbf{T}}\right) \tag{14}$$

$$\delta\boldsymbol{\epsilon}^{\mathbf{vol}} = \mathbf{I} : \delta\mathbf{D} \tag{15}$$

$$\delta\mathbf{L} = \frac{\partial\delta u}{\partial X} \tag{16}$$

$$\mathbf{S} = \boldsymbol{\sigma} + pI \tag{17}$$

$$p = -\frac{1}{3}\mathbf{I} : \boldsymbol{\sigma} = -\frac{\partial\psi}{\partial J} \tag{18}$$

Here $\mathbf{B}^* = J^{-2/3}\mathbf{B}$ is the corrected left Cauchy–Green tensor, S is the deviatoric strain tensor, δe is the virtual deviatoric strain tensor, $\delta\varepsilon^{\mathrm{vol}}$ is the virtual volumetric strain tensor, p is the hydrostatic pressure, δD is the virtual strain rate tensor, and δL is the virtual velocity gradient tensor.

Hence, the deviatoric stress with damage can be rewritten as:

$$S = \frac{2R_{\mathrm{d}}}{J}\mathrm{DEV}\left[\left(\frac{\partial\psi}{\partial\bar{I}_1} + \bar{I}_1\frac{\partial\psi}{\partial\bar{I}_2}\right)\mathbf{B}^* - \frac{\partial\psi}{\partial\bar{I}_2}\mathbf{B}^*\cdot\mathbf{B}^*\right] \tag{19}$$

$$S = \frac{2R_{\mathrm{d}}}{J}\left[\left(\frac{\partial\psi}{\partial\bar{I}_1} + \bar{I}_1\frac{\partial\psi}{\partial\bar{I}_2}\right)\left(\mathbf{B}^* - \frac{\mathrm{trace}(\mathbf{B}^*)}{3}\right) - \frac{\partial\psi}{\partial\bar{I}_2}\left(\mathbf{B}^*\cdot\mathbf{B}^* - \frac{\mathrm{trace}(\mathbf{B}^*\cdot\mathbf{B}^*)}{3}\right)\right], \tag{20}$$

Therefore, the stress (deviatoric stress and volumetric stress) with damage can be written as:

$$\sigma_{ij} = \frac{2R_{\mathrm{d}}}{J}\left[\frac{1}{J^{2/3}}\left(\frac{\partial\psi_0}{\partial\bar{I}_1} + \bar{I}_1\frac{\partial\psi_0}{\partial\bar{I}_2}\right)\mathbf{B_{ij}} - \left(\bar{I}_1\frac{\partial\psi_0}{\partial\bar{I}_1} + 2\bar{I}_2\frac{\partial\psi_0}{\partial\bar{I}_2}\right)\frac{\delta_{ij}}{3} - \frac{1}{J^{\frac{4}{3}}}\frac{\partial\psi_0}{\partial\bar{I}_2}\mathbf{B_{ik}B_{kj}}\right] + \frac{R_d\partial\psi_0}{\partial J}\delta_{ij} \tag{21}$$

and further as

$$\sigma_{ij} = \frac{2e^{-(\beta_1\tau)}}{J}\left[\frac{1}{J^{2/3}}\left(C_{10} + \bar{I}_1C_{01}\right)\mathbf{B_{ij}} - \left(\bar{I}_1C_{10} + 2\bar{I}_2C_{01}\right)\frac{\delta_{ij}}{3} - \frac{1}{J^{\frac{4}{3}}}C_{01}\mathbf{B_{ik}B_{kj}} + \frac{K_0inJ}{2J}\delta_{ij}\right], \tag{22}$$

where δ is the Kronecker delta function, and ψ_0 is the strain energy density function per unit reference volume of the intact erythrocyte membrane.

The developed erythrocyte membrane damage (EMD) model, Eq. (22), to induce localised damage in the erythrocyte membrane was implemented using the VUMAT subroutine, whereas the Mooney–Rivlin law model to describe the constitutive response of the intact erythrocyte membrane was implemented using the Abaqus materials module.

The erythrocyte membrane damage model was verified using a single–shell-element model subjected to an equi-biaxial strain of 1.1. The verification involved comparing the true stress obtained with the VUMAT subroutine and the built-in Mooney–Rivlin law for an intact erythrocyte membrane with the chemical damage parameter $\beta_1 = 0$. For this case, the constitutive responses of the developed VUMAT subroutine and the built-in Mooney–Rivlin law are expected to be identical. Thereafter, the single-shell-element model was used with various degrees of chemical damage to evaluate the stability of the developed erythrocyte membrane damage model using Drucker's stability criterion.

The material's relative compressibility also determines the mechanical response of the erythrocyte membrane. The relative compressibility is the ratio of the initial bulk modulus K_0 to the initial shear modulus μ_0 of the material:

$$R_{\mathrm{c}} = \frac{K_0}{\mu_0} \tag{23}$$

where μ_0 and K_0 are defined by Eqs. (24) and (25), respectively, and large R_{c} values show that the material is less compressible:

$$\mu_0 = 2(C_{10} + C_{01}) \tag{24}$$

$$K_0 = \frac{2}{D_1} \tag{25}$$

The Poisson's ratio ν for hyperelastic materials is related to R_{c} by:

$$\nu = \frac{3R_{\mathrm{c}} - 2}{6R_{\mathrm{c}} + 2} \tag{26}$$

The inverse bulk modulus D_1 defines the material compressibility and is expressed as:

$$D_1 = \frac{3(1-2\nu)}{2(C_{10} + C_{01})(1+\nu)} \tag{27}$$

For this study, the Poisson's ratio of the erythrocyte membrane was set to 0.499 to avoid numerical singularity; hence, D_1 was set to 12 mm^2/N. The material parameters

for the Mooney–Rivlin model are computed from the elastic modulus by:

$$C_{10} = \frac{E}{6(1+\rho)} \tag{28}$$

and $C_{01} = \rho\ C_{10}$ (Zhang & Zhang 2011). For an elastic modulus $E = 1$ kPa and $\rho = 0.1$ used in the current study, the corresponding values of C_{10} and C_{01} are 152 Pa and 15.2 Pa, respectively.

2.2.2 Tight junction

The tight junction was represented as an annulus, mimicking its function during the invasion process. The energy associated with the work done by the tight junction is not yet known. However, an estimate of the minimum energy contribution of the tight junction required for a successful invasion was determined with the developed finite element model, and the Mooney Rivlin law was used to define the mechanical response of the annulus structure. The material parameters were determined by minimising the objective function defined by:

$$F_{\mathrm{m}}(C_j) = \psi_{\mathrm{m}}(C_j) \times D_{\mathrm{m}}(C_j) \tag{29}$$

where ψ_{m} is the strain energy density function for the annulus structure, and D_{m} is the diameter of the tight junction at maximum indentation depth at the end of the invasion when the simulation step time is 1.1 s. The binary search algorithm below was used to search for material parameters that minimise the objective function in Eq. (29).

Given an array C_j of n elements C_{0j}, C_{1j}, C_{2j} …. C_{nj-1} such that $C_{0j} \le C_{1j} \le C_{2j} \le \ldots \le C_{nj-1,}$ the following pseudo-code uses the binary search algorithm to find the value of the material parameter in $\mathrm{C_j}$ that minimises the objective function.

1. Set $L_j = 0$ and $R_j = n_j - 1$
2. If $L_j > R_j$, the search terminates as unsuccessful
3. Determine the middle element index $m_j = \mathrm{floor}\ ([L_j + R_j]/2)$
4. Compute the D_{m} using the middle element parameter in C_j.
5. If $D_{\mathrm{m}} > M_{\mathrm{d}} + \bar{\mathrm{e}}$ update C_j such that $C_j \ge C_{\mathrm{m}}$, compute F_{m} and go to step 2.
6. If $D_{\mathrm{m}} < M_{\mathrm{d}} + \bar{\mathrm{e}}$, update C_j such that $C_j \le C_{\mathrm{m}}$, compute F_{m} and go to step 2.
7. If $D_{\mathrm{m}} \approx M_{\mathrm{d}}$ the search is done, and compute $F_{\mathrm{min}} = \min\ (F_{\mathrm{m}})$

here M_{d} is the width of the merozoite at maximum indentation depth, and $\bar{\mathrm{e}}$ is the clearance between the tight junction and the merozoite at the maximum indentation depth. When $F_{\mathrm{m}} = F_{\mathrm{min}} = \min\ (F_{\mathrm{m}})$ (Fig. 2a), C_j gives a minimum strain energy $\psi_{\mathrm{m}}\ (C_j)$ such that $D_{\mathrm{m}} \approx M_{\mathrm{d}}$ (Fig. 2b). The strain energy $\psi_{\mathrm{m}}\ (C_j)$ of the annulus structure increases from point a to b and c (Fig. 2a) while the diameter $\mathrm{D_m}$ decreases from point a to b but remains constant from point b to c (Fig. 2a and b).

The mechanical properties of the annulus structure that mimics the tight junction were determined by minimising the objective function, yielding Mooney–Rivlin parameters C10 = 0.04 MPa, C01 = 0.004 MPa, and $D_1 = 0.3\ \mathrm{mm^2/N}$. The determined mechanical properties represent the minimum energy required by the annulus structure to ensure erythrocyte membrane wrapping.

2.2.3 Erythrocyte cytoplasm

The smoothed particle hydrodynamics (SPH) method was used to model the erythrocyte cytoplasm deformation. Smoothed particle hydrodynamics is a fully Lagrangian mesh-free modelling scheme permitting the discretisation of a prescribed set of continuum equations by interpolating the properties directly at a discrete set of points distributed over the solution domain. This approach was first developed to solve PDE problems in astrophysics (Gingold & Monaghan 1977). In Abaqus, the SPH scheme discretises the continuum partial differential equations (Violeau & Rogers 2016). SPH uses an evolving interpolation scheme to approximate a field variable at any point in a domain. Using the particle approximation or field function Eq. (30) and its derivative Eq. (31), the Navier–Stokes equation is discretised and solved using the explicit time integration method.

$$f_i = \sum_{j=1}^{N} \frac{m_j}{\rho_j} f_j w\left(\left|r_i - r_j\right|, h\right) = \sum_{j=1}^{N} \frac{m_j}{\rho_j} f_j w_{ij} \tag{30}$$

$$\nabla \cdot f_i = \sum_{j=1}^{N} \frac{m_j}{\rho_j} f_j \cdot \nabla w\left(\left|r_i - r_j\right|, h\right) = \sum_{j=1}^{N} \frac{m_j}{\rho_j} f_j \cdot \nabla w_{ij} \tag{31}$$

where N is the total number of particles, h is the smoothing length, and r_i and r_j are the position vectors of the particle of interest and the particle in the neighbouring region, respectively. The field function f and its derivative are constructed using a smoothing or kernel function w (Wang et al. 2016, Fig. 1). Thus, the value of a variable at a particle of interest can be approximated by summing the contributions from a set of neighbouring particles, denoted by subscript j, for which the "kernel" function, w, is not zero.

In Abaqus, the erythrocyte cytoplasmic domain was converted to SPH particles by activating the built-in conversion functionality. The erythrocyte cytoplasm primarily

comprises viscous haemoglobin, mathematically described by the Navier–Stokes equation in the Lagrangian form (Ye et al. 2015). The erythrocyte cytoplasm is generally considered an incompressible Newtonian liquid, and thus, its dynamics are predicted by using the Navier–Stokes equations given by:

$$\nabla \cdot v = 0 \tag{32}$$

$$\frac{\mathrm{d}v}{\mathrm{d}t} = \frac{1}{\rho}\left(-\nabla p + \mu \nabla^2 v\right) + f_{\mathrm{ext}} \tag{33}$$

where p, v, ρ, μ, and f_{ext} represent the pressure, velocity, density, dynamic viscosity, and external force vector, respectively. SPH solves the Navier–Stokes equations by discretising the whole computational domain into a set of particles. The Mie–Grüneisen equation of state, Eq. (34), was used to model incompressible viscous laminar flow governed by the Navier–Stokes equation of motion. The volumetric response is governed by the equations of state, where the bulk modulus acts as a penalty parameter for the incompressible constraint. Since the viscosity of the erythrocyte cytoplasm is small, a small amount of shear resistance was specified in the materials module to suppress shear modes that can otherwise tangle the mesh. Here, the shear stiffness or viscosity was used as a penalty parameter. The default hourglass control was used because when the shear model is defined, the hourglass control forces are calculated based on the shear resistance of the erythrocyte cytoplasm, which provides very low shear strength, insufficient to prevent spurious hourglass modes. An equation of state is necessary for the erythrocyte cytoplasmic domain to link pressure P and density ρ. The Mie–Grüneisen equation of state used for this purpose (Monaghan 1988) is given as follows:

$$p = \frac{\rho_0 c^2 \eta_m}{\left(1-\eta_m s\right)^2}\left(1 - \frac{\eta_m \Gamma_0}{2}\right) + \rho_0 \Gamma_0 E_m \tag{34}$$

where ρ_0 is the reference density, and c is the speed of sound, $\Gamma_0 = 0$ is a material parameter, $\eta_m = 1 - \rho_0/\rho$ is the nominal volumetric compressive strain, E_{m} is internal energy per unit mass. The background pressure P_0 is added to avoid negative pressure values. The density is estimated from the particle distribution utilising the SPH interpolation. c and s define the linear relationship between the shock wave velocity, U_{s}, and the particle velocity, U_{p}, as follows:

$$U_{\mathrm{s}} = c + sU_{\mathrm{p}} \tag{35}$$

where s was set to zero such that $U_{\mathrm{s}} = c = 1000$ mm/s.

2.3 Finite element meshes

The finite element model comprised multiple components with varying element lengths: the erythrocyte membrane, the tight junction, the rigid merozoite, and the cytoplasm (Fig. 3a–d).

The tight junction has the shortest element length relative to the erythrocyte membrane and is typically used to determine stable time increments for the entire model. For the erythrocyte membrane, represented using shell elements with a thickness of 0.01 µm (Hochmuth et al. 1973), a mesh density study was performed to determine the mesh density that provides a converged solution. SPH was applied to the erythrocyte cytoplasmic domain; hence, no mesh density study was performed for the cytoplasm. However, to accurately simulate the cytoplasm using the SPH functionality, Abaqus requires more than 10000 particles. Hence, 18000 particles were generated using the particle conversion functionality.

The erythrocyte membrane was meshed with 19942 three-node triangular shell elements with reduced-time integration (S3R). The reduced-time integration algorithm provided more accurate results while reducing the running time. Conventional shell elements were preferred because, unlike continuum shell elements, which only have displacement degrees of freedom, conventional shell elements have both displacement and rotational degrees of freedom. For the erythrocyte membrane to wrap around the merozoite effectively, each erythrocyte membrane node must have both displacement and rotational degrees of freedom. Erythrocytes undergo extreme deformations as they circulate through narrow capillaries in the human body. To accurately predict erythrocyte deformation, displacement and rotational degrees of freedom must be allowed in each element. Additionally, shell elements were preferred over 3D solid elements for the erythrocyte membrane because they enable the modelling of thin features with fewer elements, thereby reducing computational time. Shell elements are also easier to mesh and less prone to negative Jacobian errors, which can result from negative element volume or distorted elements that might occur when using extremely thin solid features.

The erythrocyte cytoplasm was meshed using 841 eight-node linear brick elements with reduced integration and hourglass control (C3D8R). The mesh provides the initial spatial particle discretisation required for the SPH scheme. Seven hundred three-node 3D rigid triangular elements (R3D3) were used for the rigid merozoite, and 5535 ten-node modified quadratic tetrahedron elements (C3D10M) were used for the annulus structure of the tight junction.

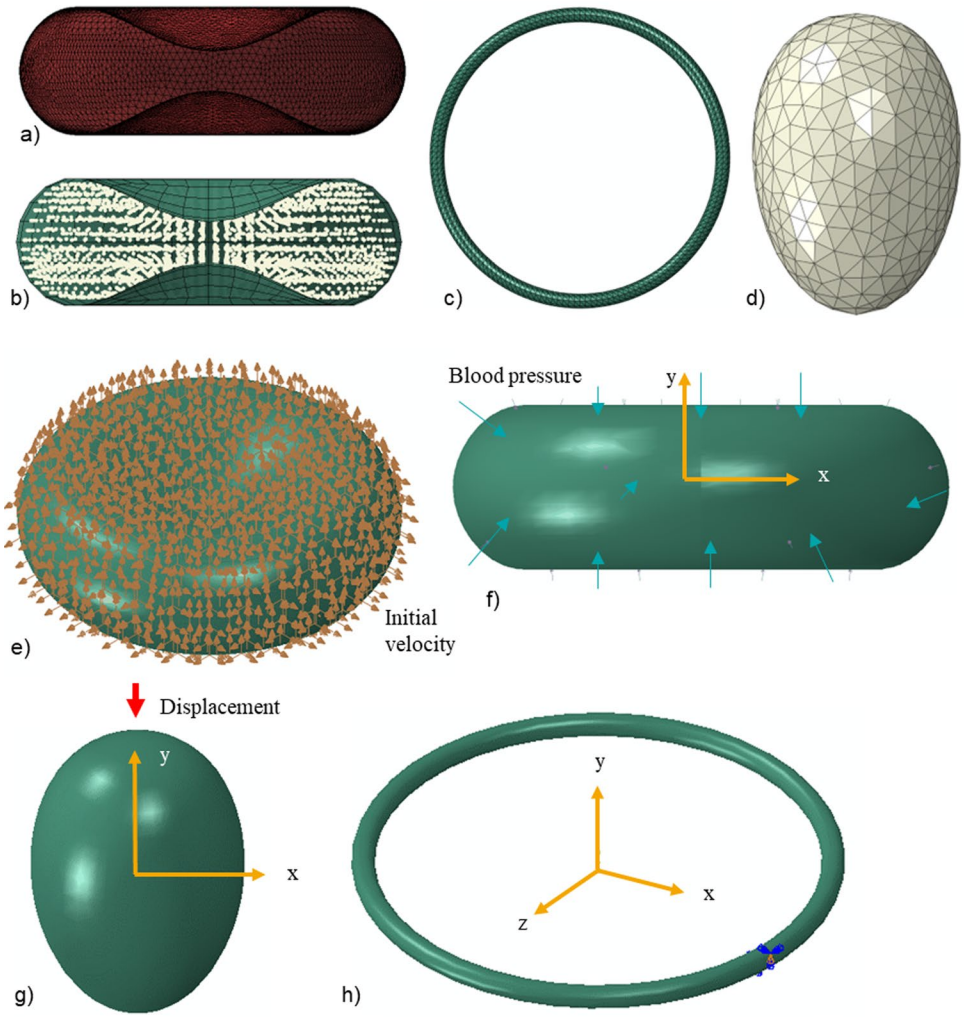

Fig. 3 Finite element meshes and boundary conditions. Finite element mesh of **a** erythrocyte membrane with triangular shell elements, **b** erythrocyte cytoplasm with 8-node linear brick elements with reduced integration and hourglass control (C3D8R), **c** annulus structure of the tight junction with ten-node modified quadratic tetrahedron elements (C3D10M), and **d** rigid merozoite with three-node 3D rigid triangular elements (R3D3). Boundary conditions: **e** Blood pressure applied on the outer surface of the erythrocyte membrane, **f** the initial velocity of 2×10^{-30} mm/s applied at each node of the erythrocyte membrane, **g** each node of the annulus structure is only allowed to displace in z and x directions, and **h** the rigid merozoite is displaced in the negative y-direction.

2.4 Boundary conditions

Several assumptions and boundary conditions were considered:

- The erythrocyte was assumed to be suspended in an Euclidean space with an initial velocity of approximately zero for each node. Initial velocity fields were pre-defined at each node of the erythrocyte membrane (Fig. 3e).
- A constant external pressure load of 16 kPa, equal to systolic blood pressure, was applied on the external surface of the erythrocyte membrane (Fig. 3f).
- The merozoite was displaced by 2 μm along its longitudinal axis. The displacement was applied using a ramp function from 0.1 to 1.1 s (Fig. 3g).
- Each node of the tight junction freely deformed in the x and z directions (Fig. 3h).

2.5 Contact interactions

Two algorithms were used to model contact interactions between structures involved in the invasion process. The general contact algorithm was used to define contact interactions between the erythrocyte membrane, the erythrocyte cytoplasm, and the tight junction. The contact pair algorithm was used to define contact between the merozoite and the outer surface of the erythrocyte membrane. The contact pair algorithm in Abaqus Explicit includes the contact surface weighting (balanced or pure master–slave) and the sliding formulation (finite, small, or infinitesimal). The contact-pair algorithm with pure master–slave weighting was used to model contact between the merozoite surface and the region of entry (ROE) on the erythrocyte membrane. In the pure master–slave scheme, the interacting surfaces can penetrate each other, leading to numerical instabilities. To avoid numerical errors due to penetration, the mesh density of the slave surface must

be greater than that of the master surface. A mesh density study was conducted for both surfaces to determine the optimal mesh sizes for the master and slave surfaces.

2.6 Model validation

2.6.1 Validation of the erythrocyte finite element model with simulation of a healthy erythrocyte in an optical tweezer/trap

The mechanical response of the erythrocyte predicted by the developed model was compared to data from an optical trap experiment during which a force of 193 pN was applied to stretch the erythrocyte (Mills et al. 2004, Fig. 7). The stretching force was applied by trapping with a laser beam one of the two silica beads attached to the erythrocyte while the second silica bead was fixed to a glass slide while the other is (Song et al. 2017). Cell stretching is performed by moving the trapped microbead. The deformation was determined from images of undeformed and stretched erythrocytes.

During the finite element simulation of the optical trap experiment, an intact erythrocyte model (i.e. without membrane damage and with $\beta_1 = \beta_2 = 0$) was subjected to an axial tensile force of $F = 200$ pN. The force was applied to the FE nodes within a circular region of 1 µm in diameter on one side of the membrane, representing the adhesion interface between the membrane and the silica bead. Rigid body motion of the erythrocyte was prevented by constraining the FE nodes of a circular region on the axially opposite membrane side, simulating the adhesion to the second silica bead. These loading and boundary conditions produced deformation of the erythrocyte in the axial and transverse directions.

2.6.2 Validation of the merozoite invasion finite element model

Recently, Geoghegan et al. (2021) used lattice light-sheet microscopy (LLSM) with high spatiotemporal resolution to analyse the merozoite invasion into the erythrocyte by segmenting and tracking the formation of parasitophorous vacuole membrane (PVM). The authors determined the portion of the erythrocyte membrane surface area that wraps the merozoite and that does not. The study documents a decrease in erythrocyte membrane surface area, as a portion of the area wraps the merozoite (Geoghegan et al. 2021, Fig. 2c). The data obtained from this study were used to validate the developed invasion model. In vivo, erythrocytes are subjected to physiological blood pressure. Hence, blood pressure must be applied to the erythrocyte model surface to obtain realistic simulation results with the invasion model. However, no physiological pressure was used in the Geoghegan et al. (2021) experiment. As such, surface area data for the erythrocyte obtained from the invasion model in which no surface pressure was applied were compared with erythrocyte areal data from the Geoghegan et al. (2021) experiment to validate the invasion model.

2.7 Finite element analysis and case studies

2.7.1 Generalised explicit finite element analysis in Abaqus

A generalised Abaqus Explicit dynamic analysis procedure was used to simulate the deformation of an erythrocyte during merozoite invasion. This procedure involves numerically solving the momentum equilibrium equation using an explicit central difference time integration rule described by Eqns. (40) and (41). The momentum equilibrium is:

$$M^{NJ}\ddot{u}_i^N = P^{NJ} - I^{NJ} \tag{36}$$

where M^{NJ} is the mass matrix, P^{NJ} is the applied load vector, I^{NJ} is the internal force vector, and $\ddot{u}_i^N$ denotes the spatial degrees of freedom. M^{NJ}, P^{NJ}, and I^{NJ} are defined as:

$$M^{NJ} = \int_V \rho_e \mathrm{H}^T \mathrm{H} dV \tag{37}$$

$$P^{NJ} = \int_V \mathrm{H}\, b_f \,\mathrm{d}V + \int_{S_0} \mathrm{H}\, t_f \,\mathrm{d}S_0 + P^{NJ}_{\text{conc}} + P^{NJ}_{\text{contact}} \tag{38}$$

$$I^{NJ} = \int_{\Omega_0} B_S\, S_P \,\mathrm{d}\Omega_0 \tag{39}$$

where ρ_e is the element density, H is the shape function of nodes, b_f is the body force per unit mass, t_f is the pressure vector component, P^{NJ}_{conc} is the concentrated nodal load, and P^{NJ}_{contact} is the nodal contact force generated automatically by Abaqus contact algorithms, B_s is the strain–displacement matrix, and S_P is the second Piola–Kirchhoff stress. M^{NJ} is diagonalised to form a lumped mass matrix, thereby reducing the computational complexity of the central difference time integration algorithm (Dassault Systèmes Simulia Corp 2015).

$$\dot{u}^N_{i+1/2} = \dot{u}^N_{i-1/2} + \frac{\Delta t_{i+1} + \Delta t_i}{2}\ddot{u}^N_i \tag{40}$$

$$u^N_{i+1} = u^N_i + \Delta t_{i+1}\dot{u}^N_{i+1/2} \tag{41}$$

The dynamic explicit analysis with mass scaling and geometrically nonlinear analysis was used. Mass scaling was only applied to the erythrocyte membrane and the tight junction to obtain a quasi-static response. The quasi-static analysis was achieved by simulating the invasion process

in the shortest time, i.e. 1.1 s, while keeping inertial forces relatively low. The semiautomatic mass scaling was used throughout the step to scale mass elements periodically and effectively reduce the wave speed. The effectiveness of the mass-scaling algorithm in ensuring a quasi-static solution was determined by confirming that the total kinetic energy of the erythrocyte model was much smaller than its internal or strain energy. Kinetic energy reflects the effects of inertia on the erythrocyte model's global response, while internal energy reflects its static effects. Time incrementation was achieved automatically by using built-in functionality. The adaptive, global estimation algorithm was applied to determine the maximum frequency of the entire model using the current dilatational wave speed.

2.7.2 Case study 1: Impact of the erythrocyte morphology on the merozoite invasiveness

Using the developed finite element model, the impact of erythrocyte morphology and merozoite-induced damage on merozoite invasiveness was assessed. The invasiveness of the merozoite in the convex region (Fig. 4a) and the concave region (Fig. 4b) was assessed by comparing the total invasion energies associated with the merozoite's invasion of the convex and concave regions. To assess the impact of sphericity, i.e. surface area-to-volume ratio, the total invasion energies were compared for the entry of the merozoite into a normal discoid-shaped erythrocyte and into a spherical erythrocyte with the same volume as the normal erythrocyte

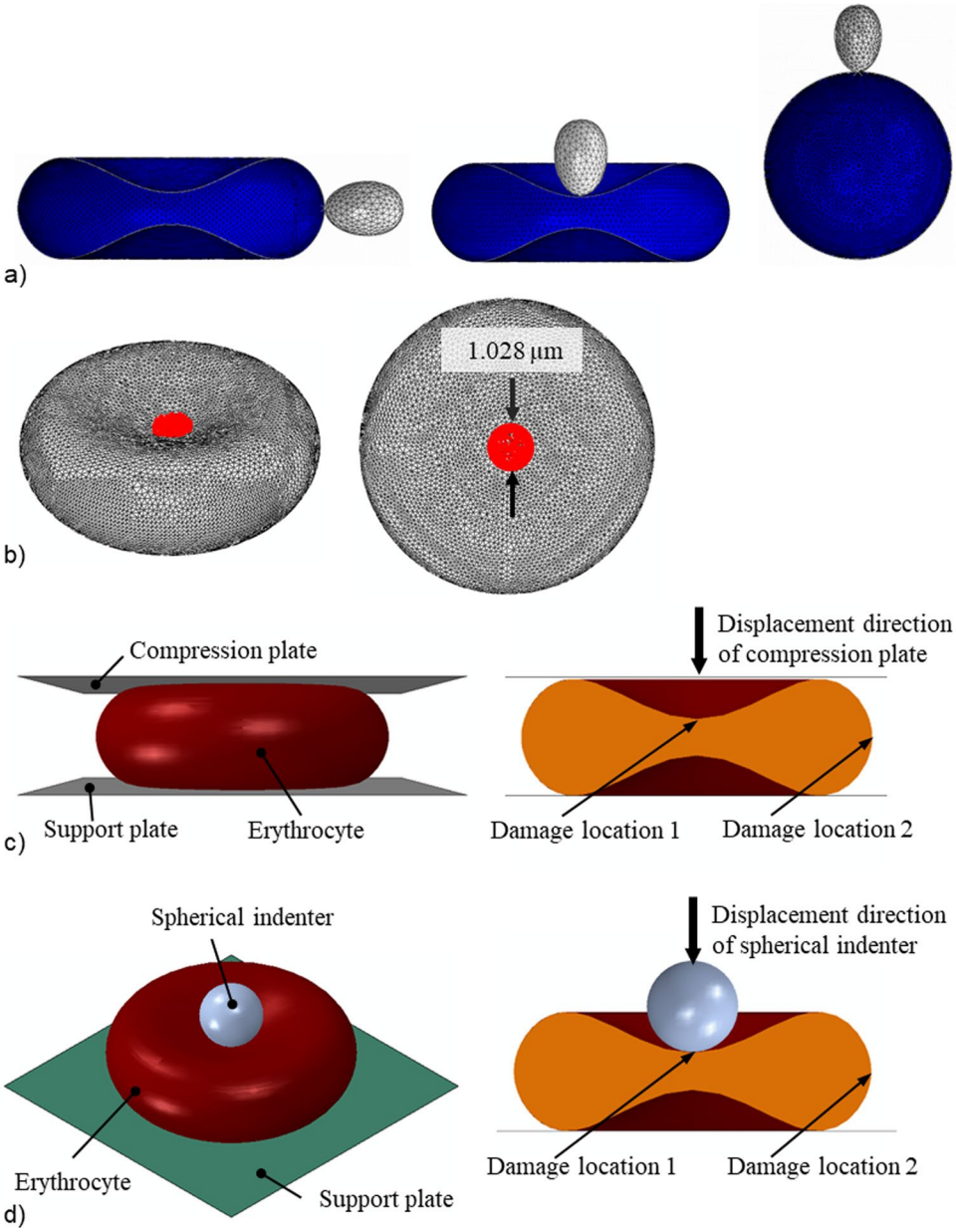

Fig. 4 **a** Case study 1: Entry point of the merozoite (grey) into a human erythrocyte (blue) in a convex (left) and concave region (middle), and into a human spherocyte (blue) (right). **b** Case study 2: Location and dimension of damage (red) induced in erythrocyte membrane. **e** Case study 3: Initial configuration of the compression test simulation (left) and locations of induced membrane damage in the concave and convex regions of the erythrocyte. **d** Case study 4: Initial configuration of the nanoindentation simulation and locations of induced membrane damage in the concave and convex regions of the erythrocyte

(Fig. 4a). To date, it is unknown whether the spherical shape impacts the invasiveness of the merozoite. The morphometric parameters used to define the two erythrocyte morphologies, i.e. discoid and spherical morphologies, are given in Table 1. The developed spherical model of the erythrocyte represents a 27% reduction of a healthy erythrocyte's surface area-to-volume ratio *(S/V)* and total surface area. With the two models of the erythrocyte, i.e. spherical and discoid models, the impact of morphological variations on the invasiveness of the malaria parasite was investigated.

2.7.3 Case study 2: Impact of phosphorylation-induced damage in the erythrocyte membrane on the merozoite invasiveness

Using the developed erythrocyte membrane damage model, the impact of the damage-induction period on merozoite invasiveness was assessed. Damage induction limited to the early invasion, i.e. $\tau = 0.1$ s, was compared to damage induction throughout the entire invasion duration of $\tau = 1.1$ s, where the amount of induced damage, $e^{\beta_1 \tau}$, was the same for both induction periods, $e^{\beta_1 \tau}|_{\tau=0.1\text{s}} = e^{\beta_1 \tau}|_{\tau=1.1\text{s}}$. Damage was induced in a central circular region of the erythrocyte membrane with a diameter of 1.028 µm (Fig. 4b). For each damage-induction period, the invasiveness of the merozoite was evaluated using the indentation force generated by the merozoite. The corresponding damage parameters used were $\beta_1 = 5.4$ and 11 for $\tau = 0.1$ s, and $\beta_1 = 0.49$ and 1 for $\tau = 1.1$ s.

2.7.4 Case study 3: Erythrocyte compression

The compression simulations with intact erythrocytes and erythrocytes with local membrane damage investigated the impact of local membrane damage on erythrocyte global mechanical and structural properties (Fig. 4c). Firstly, an intact erythrocyte model was compressed to extract the compression data. Secondly, an erythrocyte with a locally damaged erythrocyte membrane was compressed to extract two compression data sets, one obtained by inducing damage in the concave region, i.e. damage location 1, and the other in the convex region of the erythrocyte membrane, i.e. damage location 2 (Fig. 4c). The diameter of the damage region was 1.028 µm. The compression plate (10 × 10 µm) was displaced by 1.3 µm for a period of 1.1 s, while the support plate (10 × 10 µm) was fixed to facilitate compression of the erythrocyte. The compression and support plates were modelled using 5,000 linear triangular rigid shell elements (R3D3). The contact pair algorithm was used to define contact between the compression plate–erythrocyte interface and the erythrocyte–support plate interface, where surface-to-surface contact formulation with the kinematic contact method was defined. The normal and the tangential behaviour of the interfaces mentioned above were defined for this type of interaction. An isotropic tangential interaction with a negligible friction coefficient was used to describe the tangential behaviour at the interfaces. Hard contact formulation, which allows separation of the interfaces mentioned above, was used to define the normal behaviour of the interfaces. The force-compression data obtained from indenting a locally damaged and intact erythrocyte were compared to assess the sensitivity of the global indentation for local erythrocyte membrane damage. Sufficient sensitivity may indicate the potential of compression tests for further development and implementation to study merozoite-induced damage in a physical experiment. The impact of surface pressure on the mechanical response of the locally damaged erythrocyte membrane was also investigated.

Table 1 Erythrocyte parameters for case study 1

Erythrocyte shape	Surface area S (µm^2)	Volume V (µm^3)	S/V (µm^{-1})
Discoid	135	94	1.44
Spherical	98.47	94	1.05

2.7.5 Case study 4: Erythrocyte nanoindentation

The nanoindentation simulation was conducted using a similar approach to that of the compression test simulation in the previous section. The nanoindentation simulation involved an intact erythrocyte and an erythrocyte with a locally damaged membrane to investigate the impact of local membrane damage (Fig. 4d). The spherical indenter with a diameter of 2 µm, representing 25.6% of erythrocyte diameter, was displaced by 1.31 µm, representing 64.7% of the maximum erythrocyte thickness. The support plate (10 × 10 µm) was fixed to facilitate indentation of the erythrocyte. The spherical indenter was modelled using 854 linear rigid triangular shell elements (R3D3), while the support plate was modelled using 5000 linear rigid triangular shell elements (R3D3). The contact pair algorithm was used to define contact between the spherical indenter–erythrocyte interface and the erythrocyte–support plate interface, where the surface-to-surface contact formulation with the kinematic contact method was defined. Both normal and tangential behaviours of the interfaces mentioned above were defined for this type of interaction. An isotropic tangential interaction with a negligible friction coefficient was used to describe the tangential behaviour at the interfaces. Hard contact formulation that allows separation of the interfaces was used to define the interfaces' normal behaviour. The force-indentation data obtained from the locally damaged and intact erythrocytes were compared to assess the sensitivity of the nanoindentation to local erythrocyte membrane damage. A sizeable difference

between the force-indentation curves of the undamaged and damaged erythrocyte suggests that the nanoindentation test is sensitive to erythrocyte membrane damage.

Finite element simulations were conducted on the University of Cape Town High Performance Computing (HPC) facility using Abaqus on Windows-based multi-core compute nodes. CPU and memory resources were allocated through the SLURM scheduler.

3 Results

3.1 Erythrocyte membrane damage model

The true stresses defined by the Abaqus built-in Mooney–Rivlin model and the erythrocyte membrane damage model with the parameter values provided in Table 2 agreed well for the intact membrane, i.e. for $\beta_1 = 0$, and for true strain between 0 and 1.1 (Fig. 5a). This agreement indicates that the developed VUMAT subroutine was accurately implemented.

When the damage parameter was changed from the intact state with $\beta_1 = 0$ to the damaged state with $\beta_1 = 2.7$, the in-plane true stress decreased for any given true strain (Fig. 5b). For a true strain of 1.1, the in-plane true stress decreased from 0.0048 MPa for $\beta_1 = 0$ to 0.0028 MPa for $\beta_1 = 0.49$, 0.0016 MPa for $\beta_1 = 1$, and 0.00025 MPa for $\beta_1 = 2.7$.

Table 2 Material parameter values to represent an intact erythrocyte membrane with the erythrocyte membrane damage model

D_1 (mm^2/N)	C_{10} (μN/mm^2)	C_{01} (μN/mm^2)	β_1
12	152	15.2	0

3.2 Validation of the erythrocyte and invasion models

The developed erythrocyte model was validated by comparing optical tweezer experimental data (Mills et al. 2004) with numerical results from simulations of an optical tweezer experiment. When a force of 200 pN was applied diametrically, the dimension of the erythrocyte increased in the direction of the applied load, i.e. axial dimension (Fig. 6a), and decreased in the direction normal to the applied force, i.e. traverse dimension.

The increase in displacement of the erythrocyte finite element model in the axial direction leads to an increase in the axial diameter of the erythrocyte. In contrast, the increase in the transverse displacements of the erythrocyte finite element model leads to the reduction of the transverse diameter of the erythrocyte (Fig. 6a).

The numerical data show that the transverse diameter of the erythrocyte model fits well with the experimental data. However, the axial diameter of the erythrocyte model only fits well with experimental data when it is less than 0.0096 mm (Fig. 6b and c). For the erythrocyte model, the axial diameter of 0.0096 mm corresponds to the maximum principal erythrocyte membrane logarithmic strain of 1.81 (Fig. 6d). Beyond this point, the model fits experimental data in the axial direction with limited accuracy.

The invasion model was validated by comparing the erythrocyte surface area with experimental erythrocyte areal deformation data obtained by tracking and segmenting the erythrocyte membrane during the invasion process (Geoghegan et al. 2021). The erythrocyte surface area numerically predicted for the case without blood pressure agrees well with the experimental data from Geoghegan et al. (2021), which were also obtained without blood pressure on the erythrocyte (Fig. 7a). The maximum error between the experimental areal data (Geoghegan et al. 2021) and the numerically predicted data was 5.2%. Without blood

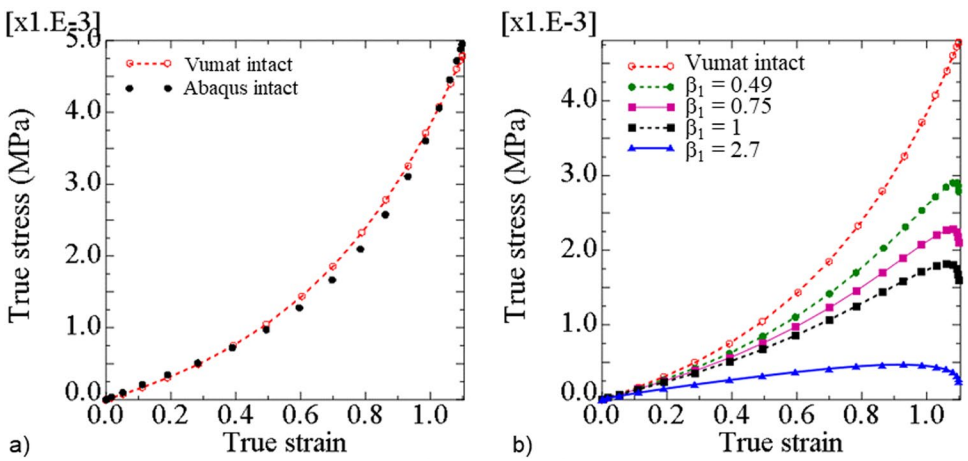

Fig. 5 **a** True stress versus true strain in a shell element determined with the Abaqus built-in Mooney–Rivlin model ('Abaqus intact') and the erythrocyte membrane damage model ('Vumat intact') for $\beta_1 = 0$, and **b** true stress versus true strain determined with the erythrocyte membrane damage model showing the stress decrease with initiation and increase of erythrocyte membrane damage from $\beta_1 = 0$ to 2.7

pressure, the model predicts a decrease in erythrocyte surface area consistent with experimental data from Geoghegan et al. (2021). In contrast, when a blood pressure of 16 kPa is applied, the erythrocyte's surface area increases during the late stages of the invasion process (Fig. 7a). The deformation of the erythrocyte model with a blood pressure of 16 kPa is entirely different from that without blood pressure (Fig. 7b and c). The largest maximum principal logarithmic strain in the erythrocyte membrane during the merozoite entry is 1.77 (Fig. 7d), which is less than the maximum principal logarithmic strain accuracy threshold of 1.81 established for the erythrocyte model.

3.3 Impact of erythrocyte morphology on merozoite invasiveness

The impact of morphological variations of the erythrocyte on the invasiveness of the merozoite is determined by the maximum amount of energy required for successful invagination of the merozoite (case study 1). When the merozoite invades a convex region of the erythrocyte, the maximum strain energy predicted by the invasion model is 0.38×10^{-15} J, whereas when it invades the concave region of the erythrocyte, the maximum strain energy of 0.238×10^{-15} J is predicted (Fig. 8a). For the invasion of a spherocyte, a maximum strain energy of 0.545×10^{-15} J is predicted, which is 43% and 129% larger than the energy required for the invagination of a merozoite in the convex and concave region of the erythrocyte, respectively.

3.4 Impact of phosphorylation-induced damage in the erythrocyte membrane on the merozoite invasiveness

The impact of malaria-induced erythrocyte membrane damage on the invasiveness of the merozoite (case study 2) is determined by the variation of the maximum indentation force required by the merozoite to invade the erythrocyte for increasing membrane damage represented by increasing β_1 from 0 to 2.7 (Fig. 8b).

For erythrocyte membrane damage, $e^{\beta_1 \tau}$, limited to the early invasion stage (i.e. for $\tau = 0.1$ s of the total simulation time of $\tau = 1.1$ s), the maximum indentation forces are lower than for an equal amount of erythrocyte membrane damage induced for the entire simulation time. For example, the damage induced for $\beta_1 = 0.49$ with $\tau = 0.1$ s is the same as for $\beta_1 = 5.4$ with $\tau = 1.1$ s. Similarly, equal damage is obtained for $\beta_1 = 1$ with $\tau = 1.1$ s and $\beta_1 = 11$ with $\tau = 0.1$ s. The maximum indentation force is larger for an intact erythrocyte membrane (22.4 pN) than for an erythrocyte with membrane damage of $\beta_1 = 0.49$ and $\tau = 1.1$ s (17 pN). When the same damage amount is induced in the erythrocyte membrane during early invagination for $\tau = 0.1$ s (with $\beta_1 = 5.4$), the maximum indentation force is yet lower (15 pN). Similarly, the maximum indentation force of 11 pN for $\beta_1 = 11$ with $\tau = 0.1$ s is lower than the force of 12.5 pN for $\beta_1 = 1$ with $\tau = 1.1$ s.

3.5 Impact of local erythrocyte membrane damage on the global mechanical responses of the erythrocyte

For compression of the entire erythrocyte (case study 3), the force–displacement curves do not differ between the normal erythrocyte and that with damage at locations 1 and 2, respectively, with $\beta_1 = 32$ for $\tau = 0.1$ s (Fig. 9a). This result shows that global compression is insensitive to local damage to the erythrocyte membrane caused by phosphorylation.

For local nanoindentation of an intact erythrocyte (case study 4), the maximum indentation force is 2.5-fold lower for damage induced at damage location 1 (i.e. the region of the indentation) (0.72×10^{-12} N) than at damage location 2 (1.78×10^{-12} N) (Fig. 9b). The latter is similar to the maximum indentation force for the intact erythrocyte membrane (1.68×10^{-12} N). An indentation displacement of 1.31 µm causes a maximum principal logarithmic strain in the erythrocyte membrane of 0.112 without blood pressure (Fig. 9c). For damage induced at damage locations 1 and 2, respectively, with $\beta_1 = 32$ for 0.1 s, the maximum principal logarithmic strain is 0.589 (Fig. 9d) and 0.24 (Fig. 9e). The surface area of the intact and the damaged erythrocytes increases equally from 135 to 137 µm^2, resulting in an areal strain of $A_{s,max} = 0.014$ (Fig. 9c to e).

4 Discussion

Although considerable progress has been made in understanding which factors determine merozoite invasiveness, most studies have not addressed the collective role of the biophysical characteristics of erythrocyte deformability in the invasion process. Cell shape, cytoplasmic viscosity, and membrane stability are the main determinants of erythrocyte deformability (Mohandas & Chasis 1993; Mohandas & Evans 1994). Experimental data on the mechanical properties of the human erythrocyte are widely available; however, it remains unknown how these physical properties influence the invasiveness of the merozoite. Hence, in the current study, an in silico approach was developed to investigate the role of erythrocyte morphology and merozoite-induced damage to the erythrocyte membrane, which are difficult to isolate experimentally, in the invasiveness of the merozoite. Importantly, this approach provides a mechanistic understanding that contributes to the rational identification of biomechanical targets for cell-mechanics-based antimalarial drug screening (Krishnan et al. 2016).

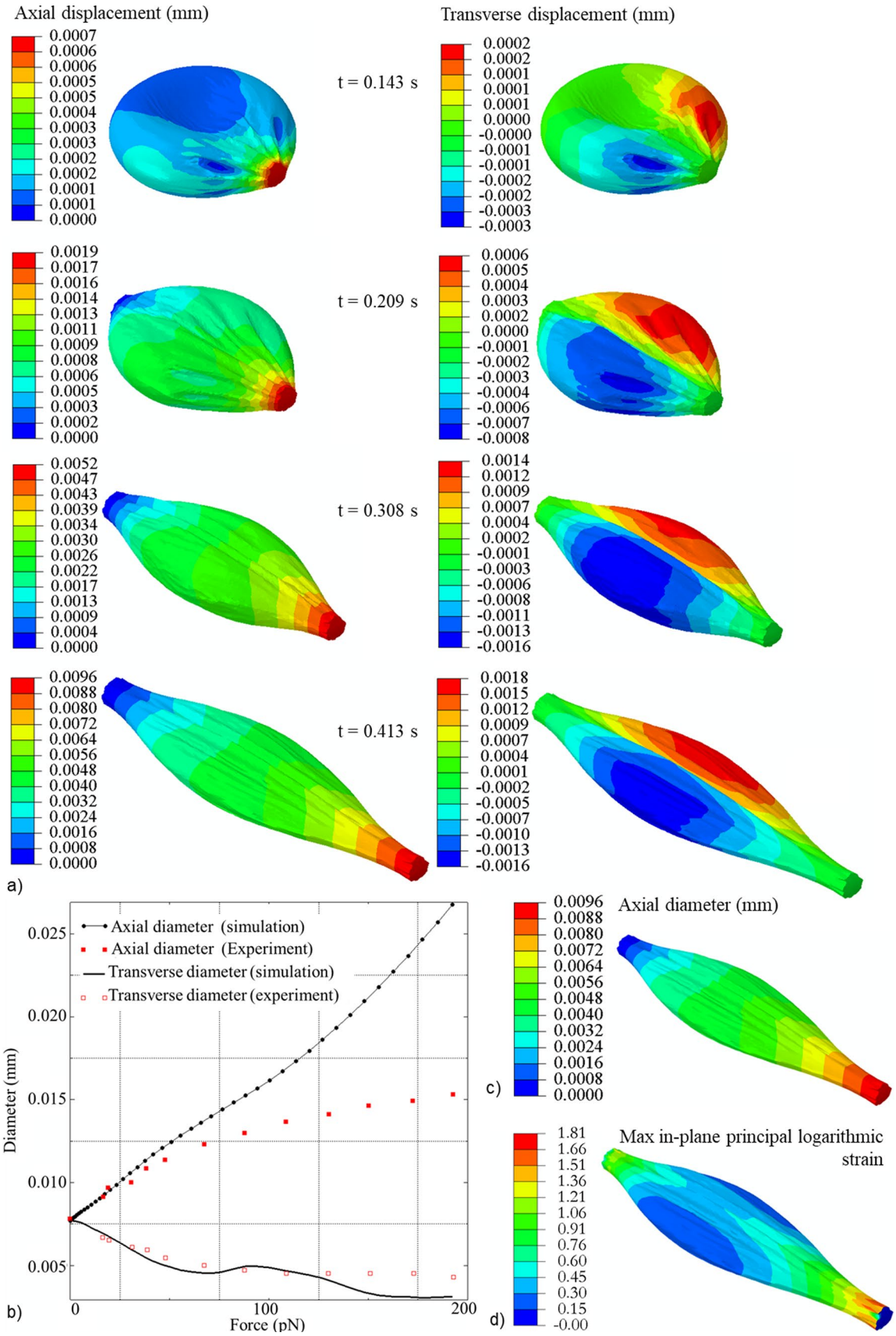
Axial displacement (mm)
Transverse displacement (mm)
t = 0.143 s
t = 0.209 s
t = 0.308 s
t = 0.413 s
a)
Axial diameter (simulation)
Axial diameter (Experiment)
Transverse diameter (simulation)
Transverse diameter (experiment)
Diameter (mm)
Force (pN)
b)
Axial diameter (mm)
c)
Max in-plane principal logarithmic strain
d)

◂**Fig. 6** **a** The contour plots of axial and transverse displacement of the erythrocyte predicted with the FEM model at 0.0143 s, 0.209 s, 0.308 s, and 0.413 s of the optical tweezer simulation. **b** Optical tweezer simulation data (axial and transverse erythrocyte finite element model diameters) for an erythrocyte without membrane damage (i.e. $\beta_1 = 0$ and $\beta_2 = 0$) fitted with experimental data for the axial and transverse diameter of a human erythrocyte from Mills et al. (2004). Contour plots of axial diameter (**c**) and maximum principal logarithmic strain (**d**) of the erythrocyte predicted with the finite element model of an optical tweezer test.

4.1 Erythrocyte membrane damage model

To date, experimental investigations of erythrocyte invasion have predominantly focused on the roles of parasite adhesins, signalling pathways, and the identity of binding receptors on the erythrocyte surface. Erythrocyte membrane damage mechanics associated with the invasion process have received limited attention (Koch et al. 2017).

The erythrocyte membrane damage model developed in the current study utilises the hyperelastic Mooney–Rivlin constitutive law, complemented with an exponential damage function to account for membrane remodelling due to phosphorylation. Despite limited knowledge of merozoite-induced damage, the model allowed for the representation of varying levels of damage. One constraint of hyperelastic constitutive models is their instability when strain is inversely related to stress. One way to assess a model's stability is using Drucker's criterion. However, this method has challenges, as some hyperelastic models can be Drucker-unstable at both small and large strains under different loading conditions. Hence, standard practice is to use a model with a known stability threshold or validity range. For example, the Mooney–Rivlin model has a known validity range for equi-biaxial logarithmic strain up to 138% (Marckmann & Verron 2006).

The stability threshold of the developed constitutive damage model was analytically determined using Drucker's stability criteria. The decrease in the maximum stress indicates a reduction in stiffness when damage is induced (Fig. 5b), indicating that the developed damage model accurately mimics the phosphorylation of the key erythrocyte membrane skeleton. The main limitation of the developed erythrocyte membrane damage model is the possible instability of the underlying Mooney–Rivlin law at low strain. Furthermore, the second invariant of the left Cauchy–Green tensor of the Mooney–Rivlin law can make the developed model unstable under certain loading conditions. However, the decrease in the erythrocyte membrane stability threshold predicted by the developed model for increasing damage amounts corresponds with reports that the phosphorylation of key proteins in the erythrocyte skeleton leads to an unstable erythrocyte membrane.

4.2 Erythrocyte and invasion finite element models

The developed erythrocyte model is a two-component model of the erythrocyte membrane and cytoplasm. The diametric dimensions of the erythrocyte predicted by the developed model for a simulated optical-trap experiment were compared with experimental data from Mills et al. (2004) to validate the erythrocyte model. The predicted transverse erythrocyte diameters agree well with the experimental transverse diameters from Mills et al. (2004). However, the predicted axial diameter fits the experimental data only for axial diameters smaller than 0.0096 mm, corresponding to a maximum principal logarithmic strain of 1.81 in the erythrocyte membrane. Beyond this threshold, the developed erythrocyte model shows limited accuracy.

The invasion model was validated by comparing the predicted erythrocyte surface area during merozoite invasion with experimental data from Geoghegan et al. (2021). Since the erythrocyte was not exposed to blood pressure during the in vitro experiments, blood pressure was neglected in the invasion model for the validation simulation. The numerically predicted surface area excludes the region of the erythrocyte membrane that is in contact with the merozoite during wrapping. To allow direct comparison of the change in surface area during the invasion, the predicted data were normalised to $\tau = 1.1$. In contrast, the experimental data were normalised to the time of 49 s required for complete internalisation of the merozoite in the erythrocyte (Geoghegan et al. 2021). The predicted and experimental erythrocyte surface areas agreed well (Fig. 7a). The validated model allows prediction of the invasion process under in vivo conditions, e.g. blood pressure acting on the erythrocyte, which may be more challenging to achieve in in vitro experiments.

The validation of the invasion model also validates the developed erythrocyte membrane damage model, as the model predictions were in good agreement with the experimental data for $\beta_1 = 11$ and $\tau = 0.1$ s. Identifying the damage parameters enables the quantification of the correct invasion forces required for the merozoite to invade the erythrocyte. The invasion model indicated a maximum principal logarithmic strain in the erythrocyte membrane of 1.77. This value is below the erythrocyte model's accuracy strain threshold of 1.81, indicating that the erythrocyte deformation during the invasion process is within the determined accuracy range of the erythrocyte model.

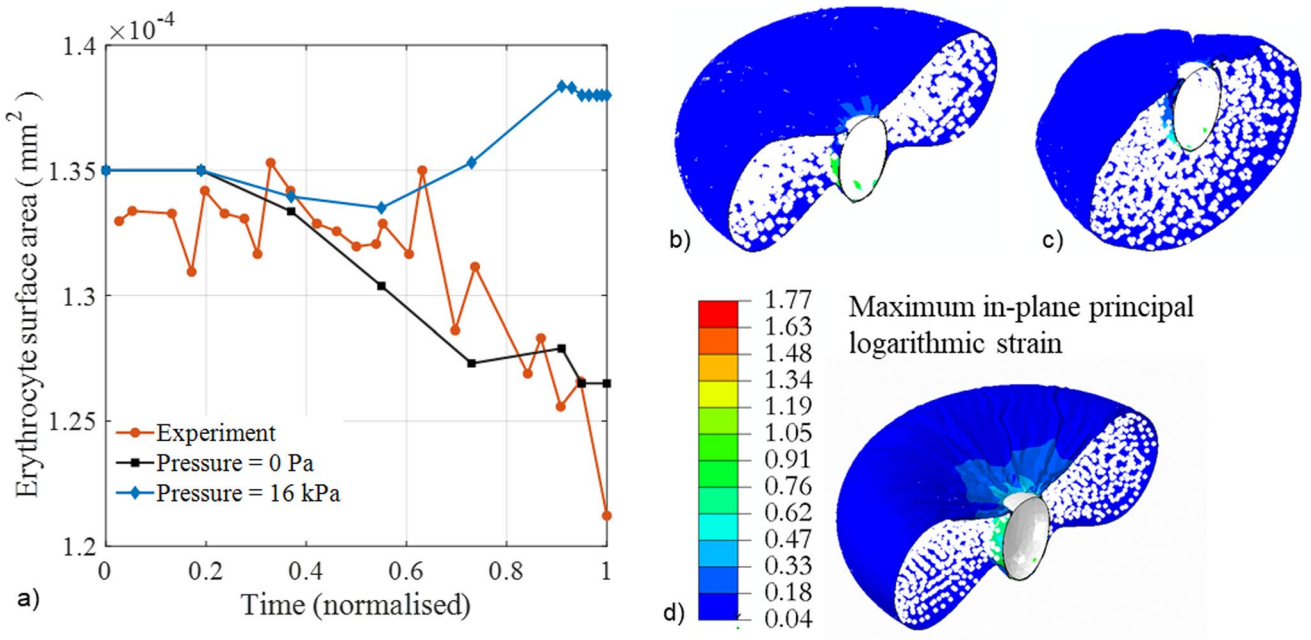

Fig. 7 **a** Variation of erythrocyte surface area during merozoite invasion predicted with the proposed invasion model with (blue diamonds) and without blood pressure (black squares), and experimental data from Geoghegan et al. (2021) (red circles) obtained without blood pressure. Erythrocyte membrane damage was modelled with $\beta_1 = 11$ induced during early invasion with $\tau = 0$ to 0.1 s. c and **d** deformation of an erythrocyte at 100% indentation depth normalised over the length of the merozoite with (**b**) and without (**c**) blood pressure applied on the outer surface of the erythrocyte. **d** Contour plot of the maximum principal logarithmic strain in the erythrocyte membrane with blood pressure at 100% normalised indentation depth

4.3 Impact of the erythrocyte morphology on the merozoite invasiveness

The implication of morphological variations of the erythrocyte on the invasiveness of the merozoite was assessed by comparing the invasion energetics for (i) a discoid erythrocyte and a spherocyte and (ii) for the concave and convex membrane regions of the discoid erythrocyte.

The merozoite entry requires lower invasion energy for the discoid erythrocyte than the spherocyte. Reducing the surface-to-volume ratio (*S*/*V*) increases the sphericity of the erythrocyte and leads to the formation of the spherocyte. The relatively low energy requirement indicates that the merozoite is more invasive when it invades a discoid-shaped erythrocyte than a spherocyte. An increase in sphericity corresponds to an increase in the energy required for the merozoite to invade the erythrocyte. The *S*/*V* of 1.44/m allows a healthy erythrocyte to undergo a large deformation of up to 230% of its original dimension. Reducing the healthy erythrocyte's *S*/*V* by 14% forms a spherocyte with a surface area of 98.5 μm^2 compared to the surface area of 135 μm^2 of a healthy erythrocyte. The discoid erythrocyte shape provides an excess surface area of 36.5 μm^2, i.e. 4.6-fold the surface area of 8.0 μm^2 of a merozoite (Dasgupta et al. 2014), sufficient to facilitate the wrapping of the merozoite. The maximum strain energy predicted by the developed finite element invasion model matches the total indentation work predicted by our analytical model (Msosa et al. 2023). The maximum strain energy of 38.0×10^{-17} J and 23.8×10^{-17} J predicted with the finite element invasion model for invasion in the convex and concave erythrocyte membrane region, respectively, is larger than the total indentation work of $E_i = 1.40 \times 10^{-17}$ J predicted by the analytical model for an areal strain of $A_{s,max} = 51\%$. The higher strain energy predicted by the finite element invasion model may be due to deformation of the erythrocyte cytoplasm, which is not accounted for in the analytical model.

Erythrocytes with membrane protein abnormalities, such as hereditary spherocytosis, are generally spherical and less deformable than normal discoid erythrocytes. However, it is unknown whether these alterations may present the merozoite with a less ideal condition for invasion of erythrocytes by merozoites. Spherocytes have been found to be less susceptible to invasion by merozoites. One reason for low susceptibility is genetic alterations in membrane proteins. However, the current study found that erythrocyte shape alteration to a spherical shape could be one of the contributing factors to the low susceptibility of spherocytes to merozoite infection.

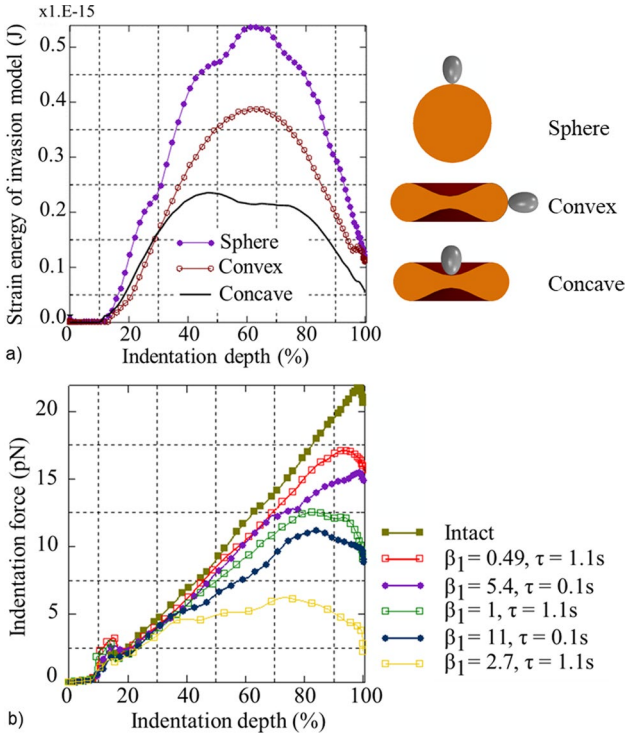

Fig. 8 **a** Required strain energy versus indentation depth predicted with the invasion model for invagination of a merozoite in the concave and convex regions of the erythrocyte and the spherocyte. **b** Indentation force versus indentation depth for varying degrees and timing of erythrocyte membrane damage.

4.4 Impact of phosphorylation-induced damage in the erythrocyte membrane on merozoite invasiveness

The impact of erythrocyte membrane damage on merozoite invasiveness was studied by inducing local erythrocyte membrane damage. The amount of damage in the erythrocyte membrane model was regulated by varying the damage parameter β_1 between 0.49 and 2.7 such that $\beta_1 = 0.49$ represented the minimum amount of damage and $\beta_1 = 2.7$ represented the maximum amount of damage. The invasiveness of the merozoite was assessed by comparing the maximum indentation forces for each value of the damage parameter β_1.

The indentation force decreases with an increase in the amount of damage in the erythrocyte membrane model (Fig. 9). This demonstrates that the merozoite invasiveness increases with the extent of damage. Merozoite-induced erythrocyte membrane damage has received limited attention, and the stages of erythrocyte membrane remodelling or damage are unknown. It is also unknown whether damage is induced only at the early invasion stage or throughout the invasion process. To validate the developed invasion model, erythrocyte membrane damage was induced at the beginning of the invasion process, i.e. at $\tau = 0.1$ s with $\beta_1 = 11$. The results suggest that erythrocyte membrane damage occurs during an early stage of invasion. The merozoite requires a greater force when damage is induced progressively throughout the invasion, i.e. for $\tau = 1.1$ s, than at the beginning of the invasion process with $\tau = 0.1$ s. These results demonstrate that the merozoite is more invasive when damage is induced during the early invasion stage ($\tau = 0.1$ s) than when it is induced progressively throughout the invasion process. Hence, regulating the timing at which the merozoite induces erythrocyte membrane damage could be a potential target for antimalarial compounds.

4.5 Impact of local erythrocyte membrane on the global mechanical responses of the erythrocyte

Compression simulations investigated the impact of local erythrocyte membrane damage on a global scale. The compression force does not differ for the intact and damaged erythrocyte, irrespective of the location of the phosphorylation damage (Fig. 9a). Hence, global compression of single erythrocytes cannot be used to detect erythrocyte membrane damage reliably. The simulations of nanoindentation of the erythrocyte in the central region indicate a discernible difference in the indentation force between an intact erythrocyte and an erythrocyte with membrane damage for damage in the central, concave region but not in the convex region of the discoid cell (Fig. 9e). This finding demonstrates that merozoite-induced local membrane damage can be detected by nanoindentation, depending on the damage location, and that further research is required.

5 Conclusions

In this study, a finite element invasion model was developed and used to (i) quantify the mechanics of a malaria merozoite's invasion of an erythrocyte and (ii) investigate the impact of erythrocyte shape and membrane damage on the invasiveness of a malaria merozoite. The findings include the smallest force required for the malaria merozoite to invade a human erythrocyte, i.e. 11 pN successfully. The invasiveness of the merozoite decreases with increasing erythrocyte sphericity, which is associated with genetic

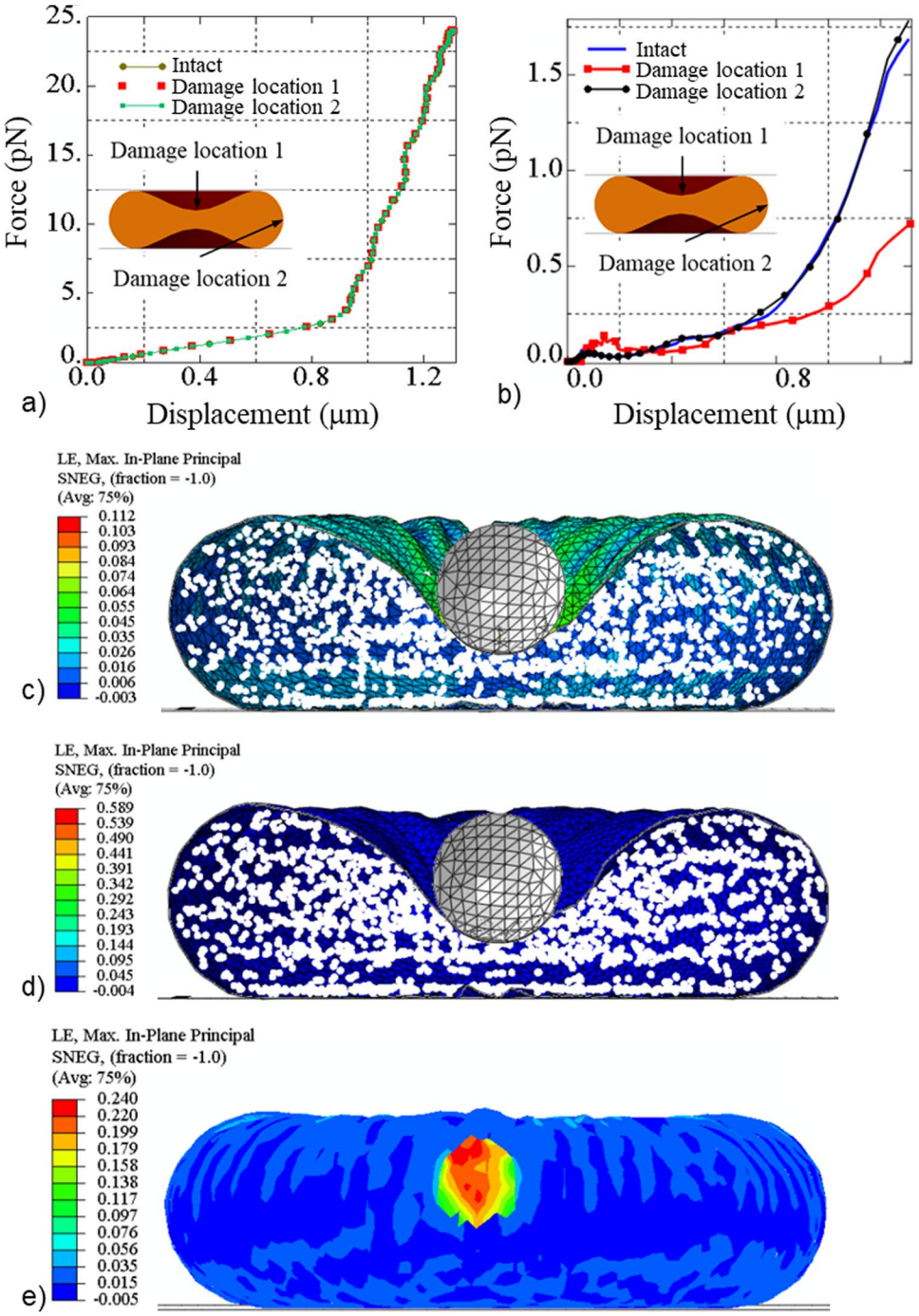

Fig. 9 Predicted force versus displacement for compression (**a**) and nanoindentation (**b**) of an intact erythrocyte and an erythrocyte damaged at damage locations 1 and 2, respectively. Maximum principal logarithmic strain for the intact erythrocyte membrane (**c**). Maximum principal logarithmic strain for the erythrocyte membrane with damage ($\beta_1 = 32$) induced for 0.1 s at damage location 1 (**d**) and 2 (**e**) where A and $A_{s,\,max}$ denote the surface area and the areal ratio of the erythrocyte, respectively

disorders such as hereditary spherocytosis. An increase in phosphorylation-induced membrane damage in erythrocytes increases the invasiveness of the malaria merozoite, as might be expected. It was further found that the malaria merozoite is more invasive when erythrocyte membrane damage induced by phosphorylation is limited to the early invasion stage, rather than throughout the entire invasion stage. The findings on invasion mechanics can guide future experimental studies to assess the merozoite's invasiveness. The results from the nanoindentation simulations indicate that nanoindentation is a suitable additional experimental technique for evaluating erythrocyte membrane damage in the context of invasion-blocking antimalarial drugs. The computational models developed for human erythrocyte and merozoite invasion can be adapted to study other parasite invasion processes.

Author contributions CM contributed to conceptualisation, data curation, formal analysis, funding acquisition, investigation, methodology, project administration, software, validation, visualisation, writing—original draft, and writing—review and editing. TA contributed to conceptualisation, methodology, project administration, supervision, and writing—review and editing. TF contributed to conceptualisation, funding acquisition, methodology, project administration, resources, supervision, validation, visualisation, and writing—review and editing.

Funding Open access funding provided by University of Cape Town. This research was supported financially by the National Research Foundation of South Africa (Grants CPRR14071676206 and IFR14011761118 to TF) and the South African Medical Research Council (Grant SIR328148 to TF), and grants from the World Bank to the University of Malawi. The funders had no role in study design, data collection and analysis, the decision to publish, or the preparation of the manuscript. Any opinions, findings, conclusions, or recommendations expressed in this publication are those of the authors and do not necessarily represent the official views of the funding agencies.

Data availability Software used and data supporting the results presented in this article are available on the University of Cape Town's institutional data repository (ZivaHub) under https://doi.org/10.25375/uct.28263767 as Msosa C, Abdalrahman T, Franz T. Software code and data for "In silico analysis of the invasion mechanics and invasiveness of the Plasmodium falciparum merozoite", Cape Town, ZivaHub, 2025, https://doi.org/10.25375/uct.28263767.

Declarations

Conflict of interest The authors declare no competing interests.

References

Abdalrahman T, Franz T (2017) Analytical modeling of the mechanics of early invasion of a merozoite into a human erythrocyte. J Biol Phys 43(4):471–479. https://doi.org/10.1007/s10867-017-9463-6

Ademiloye AS, Zhang LW, Liew KM (2018) A multiscale framework for large deformation modeling of RBC membranes. Comput Methods Appl Mech Eng 329:144–167. https://doi.org/10.1016/j.cma.2017.10.004

Ahmad IL, Ahmad MR (2015) A two component red blood cell model for single cell mechanic. Asian Res Publ Netw J Eng Appl Sci 10(19):8885–8893

Dasgupta S, Auth T, Gov NS, Satchwell TJ, Hanssen E, Zuccala ES, Riglar DT, Toye AM, Betz T, Baum J, Gompper G (2014) Membrane-wrapping contributions to malaria parasite invasion of the human erythrocyte. Biophys J 107(1):43–54. https://doi.org/10.1016/j.bpj.2014.05.024

Dassault Systèmes Simulia Corp. (2015) Abaqus 6.14 documentation—theory guide. Dassault Systèmes, Providence

Eber S, Lux SE (2004) Hereditary spherocytosis–defects in proteins that connect the membrane skeleton to the lipid bilayer. Semin Hematol 41(2):118–141. https://doi.org/10.1053/j.seminhematol.2004.01.002

Evans E, Fung Y-C (1972) Improved measurements of the erythrocyte geometry. Microvasc Res 4(4):335–347. https://doi.org/10.1016/0026-2862(72)90069-6

Fai TG, Leo-Macias A, Stokes DL, Peskin CS (2017) Image-based model of the spectrin cytoskeleton for red blood cell simulation. PLoS Comput Biol 13(10):e1005790. https://doi.org/10.1371/journal.pcbi.1005790

Flannery EL, Chatterjee AK, Winzeler EA (2013) Antimalarial drug discovery: approaches and progress towards new medicines. Nat Rev Microbiol 11(12):849–862. https://doi.org/10.1038/nrmicro3138

Geoghegan ND, Evelyn C, Whitehead LW, Pasternak M, McDonald P, Triglia T, Marapana DS, Kempe D, Thompson JK, Mlodzianoski MJ, Healer J, Biro M, Cowman AF, Rogers KL (2021) 4D analysis of malaria parasite invasion offers insights into erythrocyte membrane remodeling and parasitophorous vacuole formation. Nat Commun 12(1):3620. https://doi.org/10.1038/s41467-021-23626-7

Gilson PR, Crabb BS (2009) Morphology and kinetics of the three distinct phases of red blood cell invasion by *Plasmodium falciparum* merozoites. Int J Parasitol 39(1):91–96. https://doi.org/10.1016/j.ijpara.2008.09.007

Gingold RA, Monaghan JJ (1977) Smoothed particle hydrodynamics: theory and application to non-spherical stars. Mon Not R Astron Soc 181(3):375–389. https://doi.org/10.1093/mnras/181.3.375

Hochmuth RM, Mohandas N, Blackshear PL (1973) Measurement of the elastic modulus for red cell membrane using a fluid mechanical technique. Biophys J 13(8):747–762

Koch M, Wright KE, Otto O, Herbig M, Salinas ND, Tolia NH, Satchwell TJ, Guck J, Brooks NJ, Baum J (2017) *Plasmodium falciparum* erythrocyte-binding antigen 175 triggers a biophysical change in the red blood cell that facilitates invasion. Proc Natl Acad Sci USA 114(16):4225–4230. https://doi.org/10.1073/pnas.1620843114

Krishnan R, Park JA, Seow CY, Lee PV, Stewart AG (2016) Cellular biomechanics in drug screening and evaluation: mechanopharmacology. Trends Pharmacol Sci 37(2):87–100. https://doi.org/10.1016/j.tips.2015.10.005

Li W (2016) Damage models for soft tissues: a survey. J Med Biol Eng 36(3):285–307. https://doi.org/10.1007/s40846-016-0132-1

Li X, Peng Z, Lei H, Dao M, Karniadakis GE (2014) Probing red blood cell mechanics, rheology and dynamics with a two-component multi-scale model. Philos Trans R Soc A Math Phys Eng Sci. https://doi.org/10.1098/rsta.2013.0389

Li Y, Lu L, Li J (2016) Topological structures and membrane nanostructures of erythrocytes after splenectomy in hereditary spherocytosis patients via atomic force microscopy. Cell Biochem Biophys 74(3):365–371. https://doi.org/10.1007/s12013-016-0755-4

Lim CT, Zhou EH, Quek ST (2006) Mechanical models for living cells—a review. J Biomech Eng 39(2):195–216. https://doi.org/10.1016/j.jbiomech.2004.12.008

Marckmann G, Verron E (2006) Comparison of hyperelastic models for rubber-like materials. Rubber Chem Technol 79(5):835–858. https://doi.org/10.5254/1.3547969

Mills JP, Qie L, Dao M, Lim CT, Suresh S (2004) Nonlinear elastic and viscoelastic deformation of the human red blood cell with optical tweezers. Mech Chem Biosyst 1(3):169–180

Mohandas N, Chasis JA (1993) Red blood cell deformability, membrane material properties and shape: regulation by transmembrane, skeletal and cytosolic proteins and lipids. Semin Hematol 30(3):171–192

Mohandas N, Evans E (1994) Mechanical properties of the red cell membrane in relation to molecular structure and genetic defects. Annu Rev Biophys Biomol Struct 23:787–818. https://doi.org/10.1146/annurev.bb.23.060194.004035

Monaghan JJ (1988) An introduction to SPH. Comput Phys Commun 48(1):89–96. https://doi.org/10.1016/0010-4655(88)90026-4

Msosa C, Abdalrahman T, Franz T (2023) An analytical model describing the mechanics of erythrocyte membrane wrapping during active invasion of a *Plasmodium falciparum* merozoite. J Mech Behav Biomed Mater 140:105685. https://doi.org/10.1016/j.jmbbm.2023.105685

Ogden RW (1978) Nearly isochoric elastic deformations: application to rubberlike solids. J Mech Phys Solids 26(1):37–57. https://doi.org/10.1016/0022-5096(78)90012-1

Percário S, Moreira DR, Gomes BAQ, Ferreira MES, Gonçalves ACM, Laurindo PSOC, Vilhena TC, Dolabela MF, Green MD (2012) Oxidative stress in malaria. Int J Mol Sci 13(12):16346–16372

Pinder J, Fowler R, Bannister L, Dluzewski A, Mitchell G (2000) Motile systems in malaria merozoites: How is the red blood cell invaded? Parasitol Today 16(6):240–245. https://doi.org/10.1016/S0169-4758(00)01664-1

Preiser P, Kaviratne M, Khan S, Bannister L, Jarra W (2000) The apical organelles of malaria merozoites: host cell selection, invasion, host immunity and immune evasion. Microbes Infect 2(12):1461–1477. https://doi.org/10.1016/S1286-4579(00)01301-0

Riglar DT, Richard D, Wilson DW, Boyle MJ, Dekiwadia C, Turnbull L, Angrisano F, Marapana DS, Rogers KL, Whitchurch CB, Beeson JG, Cowman AF, Ralph SA, Baum J (2011) Super-resolution dissection of coordinated events during malaria parasite invasion of the human erythrocyte. Cell Host Microbe 9(1):9–20. https://doi.org/10.1016/j.chom.2010.12.003

Sisquella X, Nebl T, Thompson JK, Whitehead L, Malpede BM, Salinas ND, Rogers K, Tolia NH, Fleig A, O'Neill J, Tham WH, David Horgen F, Cowman AF (2017) Plasmodium falciparum ligand binding to erythrocytes induce alterations in deformability essential for invasion. Elife 6:e21083. https://doi.org/10.7554/eLife.21083

Song H, Liu Y, Zhang B, Tian K, Zhu P, Lu H, Tang Q (2017) Study of in vitro RBCs membrane elasticity with AOD scanning optical tweezers. Biomed Opt Express 8(1):384–394. https://doi.org/10.1364/BOE.8.000384

Vieira AC, Marques AT, Guedes RM, Tita V (2011) Material model proposal for biodegradable materials. Procedia Eng 10:1597–1602. https://doi.org/10.1016/j.proeng.2011.04.267

Violeau D, Rogers BD (2016) Smoothed particle hydrodynamics (SPH) for free-surface flows: past, present and future. J Hydraul Res 54(1):1–26. https://doi.org/10.1080/00221686.2015.1119209

Wang C, Wang Y, Peng C, Meng X (2016) Smoothed particle hydrodynamics simulation of water–soil mixture flows. J Hydraul Eng 142(10):04016032

Weiss JA (1994) A constitutive model and finite element representation for transversely isotropic soft tissues University of Utah]. Utah

Ye T, Phan-Thien N, Lim CT (2011) Particle-based simulations of red blood cells—a review. J Biomech 54(5):450–458. https://doi.org/10.1016/j.jbiomech.2015.11.050

Zhang Z, Zhang X (2011) Mechanical behavior of the erythrocyte in microvessel stenosis. Sci China Life Sci 54(5):450–458. https://doi.org/10.1007/s11427-011-4152-3

Zuccala ES, Satchwell TJ, Angrisano F, Tan YH, Wilson MC, Heesom KJ, Baum J (2016) Quantitative phospho-proteomics reveals the *Plasmodium* merozoite triggers pre-invasion host kinase modification of the red cell cytoskeleton. Sci Rep 6:19766. https://doi.org/10.1038/srep19766